

## Article

# Performance Evaluation of a Multifunctional Road Marking Coating for Tunnels Based on Nano SiO<sub>2</sub> and TiO<sub>2</sub> Modifications

Xiujie Quan <sup>1</sup>, Liang Yang <sup>2</sup>, Hui Li <sup>1</sup> , Yan Chen <sup>1</sup> and Shuang Shi <sup>1,\*</sup> 

<sup>1</sup> School of Transportation, Southeast University, Nanjing 211189, China; 230228856@seu.edu.cn (X.Q.); huili94@zju.edu.cn (H.L.); 220223120@seu.edu.cn (Y.C.)

<sup>2</sup> Suqian Highway Business Development Center, Suqian 223800, China; a987shi@yahoo.com.cn

\* Correspondence: shishuang@seu.edu.cn

**Abstract:** Multifunctional road marking coatings with the functions of high-temperature stability, degradation of exhaust gas, and self-cleaning are of great significance for the safe operation and environmental protection of tunnels. This article uses active acrylic resin and an organosilicon hydrophobic agent as the base material, selects expanded vermiculite and glass microspheres as insulation fillers, and uses ammonium polyphosphate, pentaerythritol, melamine, and aluminum hydroxide as high-thermal-stability systems to prepare a two-component road marking coating base material. Then, nano SiO<sub>2</sub> and modified nano TiO<sub>2</sub> are added as modifiers to prepare a multifunctional road marking coating for tunnels. The physical and chemical properties of multifunctional road marking coatings are evaluating based on laboratory tests including thermogravimetry and derivative thermogravimetry, differential scanning calorimetry, infrared spectroscopy, scanning electron microscopy, exhaust degradation, and contact angle tests. The results indicate that the developed multifunctional road marking coating effectively reduces the thermal conductivity of the carbon layer through physical changes in the flame retardant system and the heat resistance formed by the high breaking bond energy of nano SiO<sub>2</sub> during the combustion process. It forms a ceramic-like structure of titanium pyrophosphate with nano TiO<sub>2</sub> that is beneficial for improving flame retardancy without generating harmful volatile gases and has good flame retardant properties. N-V co-doping reduces the bandgap of TiO<sub>2</sub>, broadens the absorption range of visible light by nano TiO<sub>2</sub>, improves the catalytic efficiency of visible light, and achieves the degradation efficiency of the four harmful components NO<sub>x</sub>, HC, CO, and CO<sub>2</sub> in automotive exhaust by 23.4%, 8.3%, 2.5%, and 2.9%, respectively. The solid-liquid phase separation in the multifunctional road marking coating in the tunnel causes the formation and accumulation of nano SiO<sub>2</sub> and TiO<sub>2</sub> particles on the coating surface, resulting in a microstructure similar to the “micro-nano micro-convex” on the lotus leaf surface and making a water droplet contact angle of 134.2° on the coating surface.

**Keywords:** nano SiO<sub>2</sub>; nano TiO<sub>2</sub>; road marking; coating; performance



**Citation:** Quan, X.; Yang, L.; Li, H.; Chen, Y.; Shi, S. Performance Evaluation of a Multifunctional Road Marking Coating for Tunnels Based on Nano SiO<sub>2</sub> and TiO<sub>2</sub> Modifications. *Buildings* **2024**, *14*, 459. <https://doi.org/10.3390/buildings14020459>

Academic Editor: Abderrahim Boudenne

Received: 9 January 2024

Revised: 2 February 2024

Accepted: 2 February 2024

Published: 7 February 2024



**Copyright:** © 2024 by the authors. Licensee MDPI, Basel, Switzerland. This article is an open access article distributed under the terms and conditions of the Creative Commons Attribution (CC BY) license (<https://creativecommons.org/licenses/by/4.0/>).

## 1. Introduction

Road markings, as an important component of traffic safety facilities, provide drivers with guidance and management information as a carrier. They are a type of safety facility that transmits legal information to drivers and pedestrians through graphics, symbols, lines, and text to control, warn, and guide traffic. Reasonable setting of road markings can improve transportation efficiency. In addition, with the rapid development of highway construction and urban three-dimensional transportation systems in China, many long tunnels have emerged. The tunnel environment is relatively closed, and the number of vehicles has increased year by year, resulting in a sharp increase in tunnel fire accidents [1]. The road markings inside the tunnel can provide traffic safety information for extreme situations such as fires and can protect the lives of disaster victims and rescue personnel after accidents occur. At the same time, the ventilation inside the tunnel is not smooth,

making it difficult for car exhaust fumes to be discharged promptly, resulting in a significantly high concentration of exhaust gas in the tunnel. The exhaust gas contains harmful substances such as  $\text{NO}_x$ , HC, CO,  $\text{CO}_2$ , seriously endangering the health of drivers and passengers. It is necessary to degrade the exhaust gas in the tunnel. In addition, the dust and stains accumulated on the road surface inside the tunnel for a long time are difficult to clean promptly, breeding harmful microorganisms and bacteria and affecting the visibility of road markings. Therefore, multifunctional road marking coating with the functions of high-temperature stability, degradation of exhaust gas, and self-cleaning is of great significance for the safe operation and environmental protection of tunnels.

In recent years, an increasing number of experimental studies have been conducted on shield tunnel linings damaged by fire [2–6]. As road tunnels are in a semi-enclosed state, in the event of a fire, the smoke and heat generated by the fire cannot be dissipated within a short period, resulting in situations such as dense smoke, low visibility, and high temperature. All these are extremely unfavorable for escape and rescue [7–11]. Kim et al. [12] developed a fire-resistant coating consisting of cement, priming ash, and polypropylene fibers with sufficient strength to meet service load safety requirements while providing fire resistance, and the coating material was validated through fire testing using the RABT tunnel fire scenario. Alhawat et al. [13] studied the temperature and spalling behavior of tunnel linings by producing large tunnel lining prototypes using fireproof concrete with bulk fly ash and nano  $\text{SiO}_2$  (HVFNS). Researchers have extensively investigated the refractory properties of bulk fly ash (HVFA) concrete and mortar using nano  $\text{SiO}_2$  [14,15]. The results showed that the addition of nano  $\text{SiO}_2$  to cement pastes significantly improved the thermal stability of the cement system. Nano  $\text{SiO}_2$ -added samples show less strength loss after 500 °C compared to samples with silica powder [16]. Pereyra et al. [17] chose nanostructured self-curing inorganic silicates (high silica-to-alkali ratio) as the film-forming material, and the results showed that the non-polluting coating system has excellent corrosion resistance and good high-temperature stability. Zinc phytate (ZnPA) chelated geopolymer and in situ polymerized chitosan oligosaccharide (COS)/DOPO were explored as a challenging and exciting flame-retardant organic–inorganic hybrid coating using the sol–gel method, and the results showed that ZnPA addition (0.5 wt%) enhanced the flame-retardant properties of geopolymer coatings [18]. Ng et al. [19] highlighted the thermal decomposition and fire-protective behavior of two polymer-based coatings for concrete, which creates a steep temperature gradient between the coating surface and the coating–concrete interface. Abniki et al. [20] prepared a novel flame-retardant coating material using a modification of epoxy resin with phenylboronic acid in the presence of tetra-n-butyl ammonium bromide catalyst during reaction at 80–120 °C.

Nano  $\text{TiO}_2$ , as a photocatalyst, has attracted widespread attention due to its excellent photochemical properties, good stability, low cost, and non-toxic properties. It has been widely applied and studied in areas such as air purification and sewage treatment. To further improve the absorption rate of visible light by nano  $\text{TiO}_2$ , metal ion doping and non-metal ion doping modification were commonly used to modified nano  $\text{TiO}_2$ . Metal ion modification of nano  $\text{TiO}_2$  can cause lattice defects in  $\text{TiO}_2$  and improve the crystallinity of the catalyst, introducing doping energy levels into the bandgap of  $\text{TiO}_2$ , extending the absorption band edge. The method of metal non-metal co-doping has been a hot research topic in recent years. The use of dual elements to dope and modify  $\text{TiO}_2$  aims to improve the photocatalytic activity of  $\text{TiO}_2$  through different mechanisms of synergistic effects between co-doped ions. Due to the synergistic effect of ions, not only does it improve the photocatalytic activity, but it also extends the  $\text{TiO}_2$  absorption spectrum to the visible light region, improving its photocatalytic ability under visible light and making the catalytic effect more obvious. The composite-modified nano  $\text{TiO}_2^{3+}$ , N, and  $\text{WO}_3$  containing Fe have good exhaust gas degradation efficiency under special lighting conditions in highway tunnels, which can promote the improvement of the driving environment in highway tunnels [21]. Because the light sources in highway tunnels do not generate ultraviolet light, nano  $\text{TiO}_2$  cannot be used for photocatalysis. Therefore, researchers used modified

nano TiO<sub>2</sub> to improve its photocatalytic performance in the visible light range [22–24]. Zhang et al. [25] designed an innovative photocatalytic microsurface mixture (PMM) reinforced with polypropylene (PP) fibers and nano TiO<sub>2</sub> to purify severe air pollution in traffic-intensive urban areas and tunnels. Xia et al. [26] [27] investigated TiO<sub>2</sub> aqueous coatings using photocatalytic oxidation to degrade pollutants under visible and ultraviolet (UV) light. To improve the efficiency and durability of semiconductor photocatalysts for degrading automobile exhaust fumes, Liu et al. [28] designed a highly active degradation microcell by cross-linking nano TiO<sub>2</sub>, wherein the finely crumbled rubber surface was coated with a coupling agent.

The hydrophobicity of the coating surface is related to its surface wettability, which is mainly influenced by the surface roughness and compound composition. Improving the surface roughness and reducing the surface energy can significantly enhance the surface hydrophobicity. Hydrophobic surfaces not only have self-cleaning properties but also have waterproof, anti-corrosion, anti-adhesion, and anti-UV properties. The surface of lotus leaves exhibits excellent hydrophobicity and self-cleaning capabilities, mainly due to the synergistic effect of their dual micro rough structure and low-surface-energy plant wax. According to lotus leaves and rice leaves, it is proposed that micro/nano second-order rough structures are the fundamental reason for hydrophobicity. Based on this, various methods for constructing rough structures have been developed to achieve biomimetic hydrophobic self-cleaning methods such as the electrochemical method, etching method, vapor deposition method, self-assembly method, sol-gel method, etc. However, these methods often require expensive equipment and complex processes to be implemented, and they cannot be produced on a large scale, resulting in significant limitations. The nanoparticle filling method, which has emerged in recent years, is a relatively simple method for preparing superhydrophobic surfaces and is expected to overcome the aforementioned difficulties. Lu et al. [29] prepared epoxy-modified silicone resin by blending method and hydrophobically modified TiO<sub>2</sub> using a polytetrafluoroethylene (PTFE) coating method to provide raw material support for self-cleaning pavement coatings. Jiang et al. [30] modified the surface wettability of TiO<sub>2</sub> using electron-beam irradiation-initiated graft polymerization using 3-methacryloyloxypropyltrimethoxysilane (MPS) and dodecafluoroheptyl methacrylate (DFHMA) with methacrylic acid methacrylate as the modifier. Through fluoride modification, TiO<sub>2</sub> reached a superhydrophobic state and enhanced anti-icing properties [31–33]. Superhydrophobic modification of TiO<sub>2</sub> can also occur through fluorinated deposition of fluoride plasmas produced by thermal decomposition of polytetrafluoroethylene in nitrogen. Due to the grafting of groups such as \CF<sub>3</sub>, \CF<sub>2</sub>, and CH<sub>2</sub>CF<sub>2</sub> on the surface of the treated TiO<sub>2</sub>, the contact angle exceeds 150° and a superhydrophobic state is achieved [34]. Xia et al. [35] used surface-modified TiO<sub>2</sub> with stearic acid under ethanol conditions to obtain hydrophobic TiO<sub>2</sub>.

Based on the above literature analysis, this study plans to use a two-component road marking material based on active acrylic resin and organosilicon hydrophobic agent as a base material, selects expanded vermiculite and glass microspheres as insulation fillers, and selects ammonium polyphosphate, pentaerythritol, melamine, and aluminum hydroxide as flame-retardant materials, followed by the addition of nano SiO<sub>2</sub> and modified nano TiO<sub>2</sub> as modifiers to prepare a multifunctional road marking coating for tunnels. Tests such as thermogravimetry and derivative thermogravimetry (TG-DTG), differential scanning calorimetry (DSC), infrared spectroscopy (FTIR) analysis, scanning electron microscopy (SEM), the exhaust gas degradation test, and contact angle measurement were conducted to obtain various physical and chemical properties of multi-functional road marking coating in tunnels.

## 2. Preparation of Materials and Test Methods

### 2.1. Preparation of Materials

A two-component road marking material was fabricated using active acrylic resin and an organosilicon hydrophobicity agent was used as a base material. Expanded vermiculite

and glass microspheres were selected as insulation fillers. Ammonium polyphosphate, pentaerythritol, melamine, and aluminum hydroxide were selected as flame-retardant materials. Then, nano SiO<sub>2</sub> and modified nano TiO<sub>2</sub> were added as modifiers. Finally, a multifunctional road marking coating for tunnels was prepared using high-speed stirring for 30 min. Among them, the mass content of each component in units of 100 g is shown in Table 1, and the prepared marking coating material was added to a blender to mix and prepare a white semi-viscous liquid as shown in Figure 1.

**Table 1.** Raw Material Ratio.

Ingredient	Content (%)	Provenience	Ingredient	Content (%)	Provenience
Polyacrylic Resin Component A	19.73	Xuchuan Chemical (Suzhou) Co., Ltd., Suzhou, China	Ammonium Polyphosphate	3.99	Sinopharm Chemical Reagent Co., Ltd., Shanghai, China
Curing agent component B	15.51	Xuchuan Chemical (Suzhou) Co., Ltd., Suzhou, China	Pentaerythritol	3.46	Sinopharm Chemical Reagent Co., Ltd., Shanghai, China
Aluminum Hydroxide	7.24	Zibo Aotai new material technology CO., Ltd., Zibo, China	Melamine	3.24	Sinopharm Chemical Reagent Co., Ltd., Shanghai, China
Expanded Vermiculite	2.16	Nantong Xingchen Synthetic Material, Co., Ltd., Nantong, China	Reagent	7.82	Jiangsu Baoying Asphalt Technology Co., Ltd., Baoying, China
Modified nano TiO <sub>2</sub>	10.46	Jiangsu Chuangwei Transportation Technology Development Co., Ltd., Nanjing, China	Silicone Water Repellent	13.94	Nantong Xingchen Synthetic Material, Co., Ltd., Nantong, China
Glass Beads	3.48	Jiangsu Chuangwei Transportation Technology Development Co., Ltd., Nanjing, China	Nano SiO <sub>2</sub>	8.97	Nantong Xingchen Synthetic Material, Co., Ltd., Nantong, China



**Figure 1.** Modified nano TiO<sub>2</sub> and nano TiO<sub>2</sub> co-emulsions.

Modified nano TiO<sub>2</sub>, which was nitrogen–vanadium co-doped nano TiO<sub>2</sub>, was chosen for use in the sol–gel method, with the optimal doping amount of nitrogen and vanadium chosen for monodoping selected as the amount for co-doping; thus, the doping concentration of nitrogen was 3.0% and vanadium was 1.0%, the calcination temperature was 400 °C, and the N–V co-doped nano TiO<sub>2</sub> was prepared as follows:

(1) A certain amount of urea (N doping concentration of 3.0%) was added to 30 mL of anhydrous ethanol at room temperature with continuous stirring, and 17 mL of butyl titanate was added slowly with stirring for 30 min to obtain a yellow uniform and transparent solution A.

(2) Measures of 28 mL of anhydrous ethanol and 20 mL of glacial acetic acid were mixed at room temperature; a certain amount of ammonium metavanadate (V doping amount of 1.0%) was added to 8 mL of distilled water in a water bath, stirring and heating until the ammonium metavanadate was completely dissolved in the deionized water; the two solutions were then fully mixed to form solution B, and the resulting solution was placed in a dispensing funnel for spare.

(3) Under the condition of a constant temperature of 30 °C, solution B was added to solution A at a constant rate (1–2 drops per second) with continuous stirring to produce a yellow sol.

(4) The stabilized sol obtained was aged at room temperature for 7 days to form a gel.

(5) The gel was dried at 80 °C for 24 h, milled, and calcined at 400 °C for 2.5 h to obtain N–V modified nano TiO<sub>2</sub> and expressed as TiO<sub>2</sub> + N3.0% + V1.0%.

The specific steps are shown in Figure 2.

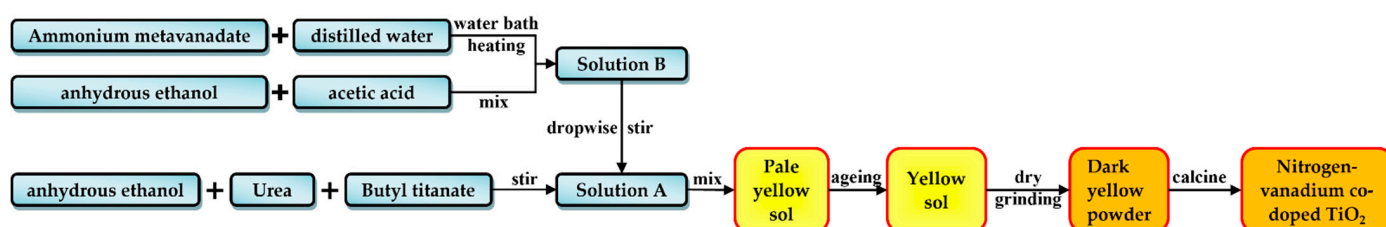


**Figure 2.** Preparation of N–V co-doped nano TiO<sub>2</sub>.

## 2.2. Test Methods

### 2.2.1. Flame Retardant Tests

TG-DTG, DSC, FTIR, and SEM tests were conducted to evaluate the flame retardancy of multifunctional road marking coating in tunnels.

#### (1) TG-DTG tests

The TG-DTG test aims to make the sample under the control of a certain temperature program and observe the change process of the mass of the sample with temperature or time. The TA910S synchronous thermal analyzer was used when testing. A measure of  $6.5 \pm 0.5$  mg of the sample was weighed and placed in an Al<sub>2</sub>O<sub>3</sub> crucible. Under the conditions of N<sub>2</sub> carrier gas, a flow rate of 20 mL·min<sup>-1</sup>, and a pyrolysis temperature of 30–800 °C, it was placed in a microbalance of the synchronous thermal analyzer for testing. The heating rate was 5, 10, 15, 20, and 25 K·min<sup>-1</sup>.

#### (2) DSC tests:

The DSC test can characterize the physical or chemical change process by measuring the change in its thermodynamic properties. It is a thermal analysis method to measure the relationship between the power difference of the input sample and the reference substance and the temperature under the condition of programmed temperature control. The information recorded during the experiment was the heat difference between the sample and the reference sample while maintaining the same temperature. A TA-Q20 differential scanning calorimeter was used to test multifunctional road marking coating in tunnels. Measures of 5–10 mg of samples were taken, with a testing temperature of 30–800 °C, a heating rate of 10 °C/min, and a N<sub>2</sub> flow rate of 40 mL/min.

#### (3) FTIR tests

The FTIR test involves the use of the interferometer interference frequency modulation working principle. The light is emitted by the light source through the Michelson interfer-

ometer into interference light, and then the interference light irradiates the sample; then, the receiver receives the interference light with sample information, and Fourier transform is used to obtain the sample spectrum. In this study, an IRAffinity-1SWL Fourier transform infrared spectrometer was employed to test the multifunctional road marking coating in the tunnel, and transmission technology was used for testing, with a resolution of  $4\text{ cm}^{-1}$ .

#### (4) SEM tests

SEM is a method of grating scanning on the surface of the sample after focusing the electron beam emitted by the electron gun. It observes and analyzes the composition, morphology and structure of the sample surface by detecting the signal generated by the electron acting on the sample. In this study, the microstructure of the carbon layer of the burned sample was obtained using a JEM-2100 (HR) field emission transmission electron microscope.

#### 2.2.2. Exhaust Degradation Tests

In this study,  $\text{TiO}_2$  was modified to purify automobile exhaust fumes under tunnel illumination conditions. Due to the influence of tunnel traffic, the  $\text{TiO}_2$  degradation effect was tested in the tunnel, and the safety of testers could not be guaranteed. Therefore, it was difficult to directly test the effect of photocatalytic materials on automobile exhaust degradation in the tunnel. Therefore, the test was carried out indoors according to the actual situation of the tunnel, and the basic conditions in the tunnel were poor lighting conditions and poor ventilation. According to these basic requirements, purification efficiency test equipment was made.

The test equipment for automobile exhaust gas purification was shown in Figure 3. The device was mainly composed of the following parts: an automobile exhaust analyzer, reaction box, ordinary incandescent lamp, ultraviolet lamp, filter dryer, gasoline engine, sample table, and negative pressure hole (vacuum) reaction box. The negative-pressure hole reaction box was the core part of the test equipment, the external dimensions were length (680 mm)  $\times$  width (530 mm)  $\times$  height (530 mm), and the volume of the whole reaction chamber was 162.5 L. The high-precision automobile exhaust analyzer has automatic zero adjustment, cleaning, temperature and pressure compensation and other functions, fully in line with the accuracy requirements of this test. An ultraviolet lamp was used in this experiment to study the degradation effect of the modified sample on the tail gas under ultraviolet light. Incandescent lamps were used to study the degradation effect of modified samples on exhaust gas under simulated tunnel lighting conditions. A gasoline engine was used to create automobile exhaust fumes ( $\text{NO}_x$ , HC, CO, and  $\text{CO}_2$ ). A vacuum pump was used to give the reaction box negative pressure and thus make it easy to exhaust gas into.

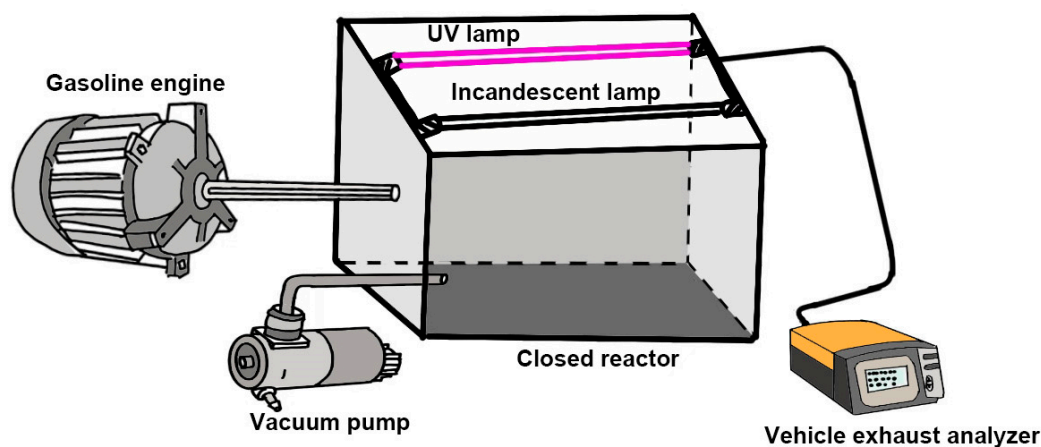


**Figure 3.** Experimental apparatus schematic diagram for photocatalytic activity test of  $\text{TiO}_2$  samples to vehicle exhaust.

The test steps were as follows: (1) start the exhaust gas analyzer: firstly, carry out the leakage test, prepare for the test, and then connect the detection probe of the exhaust gas analyzer and exhaust gas collection with the degradation device and the gasoline engine exhaust pipe; then, carry out exhaust gas collection with the degradation device intake valve. (2) Put in the specimen: put the photocatalyst into the test chamber. To make full contact between the sample and the light source, the modified nano TiO<sub>2</sub> photocatalytic material was evenly spread on the sample table, and the reaction box was sealed and ready for testing. (3) Exclude air: turn on the vacuum pump so that the reaction box is in a semi-vacuum state. (4) Pass the air into the car exhaust gas: the exhaust gas used for the test comes from the exhaust gas of the small gasoline engine when it is working; the gasoline engine is first started, and when it is in stable operation, the gas is then discharged into the reaction box. (4) Record the results of the specimen: turn on the ordinary incandescent lamp or ultraviolet light source, record the initial concentration of each gas, and exit the test state, and then start the test mode once every 10 min to collect the data until 60 min to end a group of tests.

### 2.2.3. Self-Cleaning Tests

#### (1) Self-cleaning performance tests

The self-cleaning performance test was conducted according to GB/T31815-2015 [36], using the collection of dust landing on leaves, the preparation of rainwater effluent to simulate the precipitation environment indoors, and the preparation of test boards coated with multifunctional road marking coating in tunnels. A test board without multifunctional coating was selected as the comparison board, and the multifunctional coating was applied to two test boards. Then, the prepared rainwater effluent was uniformly sprayed on the surfaces of the other two test boards, and the specimen boards were placed in a ventilated condition to dry naturally for 2 h. The test was conducted once a day according to the above steps five consecutive times. The comparison board and the two tested test boards were compared to observe the color depth and density of the sewage stains on the coating surface and visually assess the sewage stain rating of the test boards.

#### (2) Water droplet contact angle tests

In addition, a water droplet contact angle tester was used to test the contact angle of the surface of multifunctional road marking coating in tunnels. The prepared tunnel multifunctional road marking coating samples were tested in the standard environment using the hanging drop method, with a drop of deionized water on the surface of the coating and the use of image analysis technology to measure the size of the contact angle between the water droplets and the surface of the tunnel multifunctional road marking coating specimens; each sample was measured three times, taking the average value for the final measurement results. According to the size of the contact angle, used to analyze the wetting of the water droplets and the surface of the multifunctional road marking coating in the tunnel, when the water droplets and solid contact angle are present for the complete wetting phenomenon,  $\theta < 90^\circ$  indicates the hydrophilic wetting phenomenon; otherwise, it is the hydrophobic wetting phenomenon.

## 3. Results and Discussion

### 3.1. Evaluation of Thermal Stability

Tunnels constitute a semi-enclosed environment; the high-temperature stability of the material is related to its service life. To explore the effect of modified titanium dioxide and silica addition on the thermal stability of road marking, and to clarify its high-temperature stability performance, thermogravimetry analysis–differential scanning calorimetry–Fourier transform infrared spectroscopy (TG-DSC-FTIR) coupling technology was used to compare and analyze the thermomechanical properties of road marking base material and modified multifunctional marking.

### 3.1.1. TG-DTG Results Analysis

The thermal decomposition process of multifunctional road marking coatings is relatively complex. Its substrate is composed of active acrylic resin, an organosilicon hydrophobic agent, ammonium polyphosphate (APP), pentaerythritol (PER), melamine (MEL), and aluminum hydroxide ( $\text{Al}(\text{OH})_3$ ). Modified nano titanium dioxide and silicon dioxide are used as additives to endow road marking coatings with multi-functionality. TG and DTG curves and typical decomposition parameters are used to analyze and study the thermal stability performance of multifunctional road marking coatings. The results are shown in Figure 4.

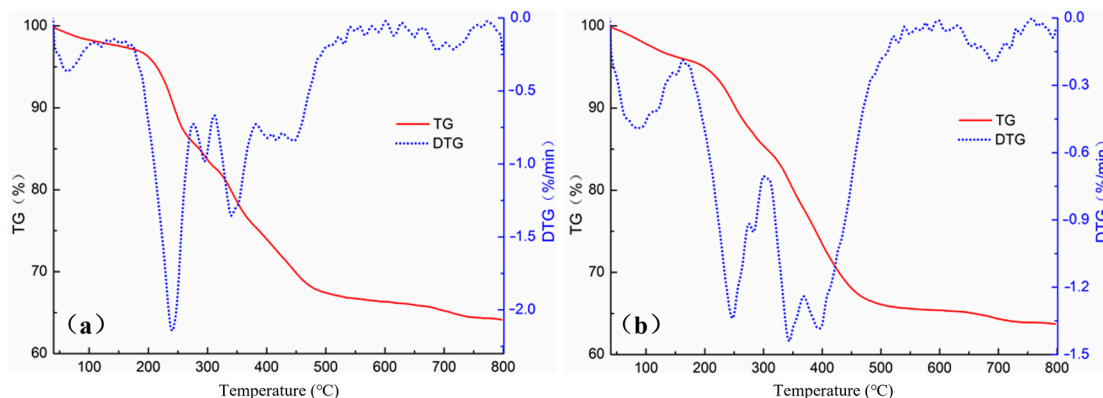


**Figure 4.** Thermogravimetric and micro commercial thermogravimetric profiles of multifunctional road marking coatings: (a) base material; (b) modified.

As can be seen from Figure 4a, when the temperature is lower than  $143.1\text{ }^{\circ}\text{C}$ , the road marking base material loses very little weight, about 2.3%, and the specimen shows a strong heat absorption peak at  $64.3\text{ }^{\circ}\text{C}$ , which is mainly due to a small amount of water being released from the tunnel road marking; the most important weight loss process of the specimen occurs in the second stage of combustion ( $143.1\text{--}275.8\text{ }^{\circ}\text{C}$ ), and the weight loss of the stage is about 11.7%. The weight loss in this stage is about 11.7%, and the maximum heat loss rate is  $-2.3\%/ \text{min}$ , mainly because in this stage APP is decomposed slowly by heat,  $\text{NH}_3$  begins to escape, and a small amount of PE begins to be oxidized to liberate water and carbon dioxide; at this stage,  $\text{Al}(\text{OH})_3$  in the coating also begins to decompose by absorbing heat, and it releases crystalline water, which evaporates at a high temperature.

The maximum thermal weight loss rates of the coatings in the third and fourth stages were  $-1.1\%/ \text{min}$  and  $-1.5\%/ \text{min}$ , respectively, and the temperature intervals in which the two stages were located were the temperature bands in which the PER and MEL in the coatings were fully reacted, with the PER starting to decompose at  $270\text{ }^{\circ}\text{C}$ , completing its decomposition at  $345\text{ }^{\circ}\text{C}$  and reaching the maximum value of its weight loss rate at  $315\text{ }^{\circ}\text{C}$ , with the MEL starting to decompose at  $296\text{ }^{\circ}\text{C}$ , completing its decomposition at  $370\text{ }^{\circ}\text{C}$ , with its weight loss rate reaching the maximum value of its weight loss rate at  $365\text{ }^{\circ}\text{C}$ . The decomposition of MEL starts at  $296\text{ }^{\circ}\text{C}$  and finishes at  $370\text{ }^{\circ}\text{C}$ , and its weight loss reaches its maximum value at  $365\text{ }^{\circ}\text{C}$ . APP as a carbonization promoter will participate in these two stages throughout, with a large amount of APP decomposition to produce  $\text{NH}_3$ , water and phosphoric acid, and then dehydration reaction to produce pyrophosphoric acid, followed by dehydration to carbon formation reaction with PER to produce a carbon layer in the molten state; at the same time, MEL is also subjected to heat to react and release  $\text{NH}_3$ , so as to produce a multi-hollow carbon layer inside the carbon layer in the molten state:  $310\text{--}325\text{ }^{\circ}\text{C}$  for the  $\text{Al}(\text{OH})_3$  dehydration reaction stage as in Equation (1), which mainly occurs in the third stage, and  $350\text{--}400\text{ }^{\circ}\text{C}$  for the formation of  $\text{Al}_2\text{O}_3$  reaction as in Equation (2), which mainly occurs in the fourth stage;  $\text{Al}(\text{OH})_3$  releases water from crystallization, and a large amount of heat is absorbed in the process of high-temperature evaporation, which promotes the high-temperature stability of the coating, and since the

maximum rate of heat weight loss of both PER and MEL occurs in the fourth stage, the maximum rate of heat weight loss in this stage is greater than the maximum heat weight loss rate of the third stage. The maximum thermal weight loss rate in this stage is greater than that in the third stage because the maximum weight loss rate of both PER and MEL occurs in the fourth stage, and the weight loss of the coating in the fifth stage mainly comes from the remaining APP and the complete decomposition of  $\text{Al}(\text{OH})_3$ .



Comparing with Figure 4b, it can be seen that the first stage of the multifunctional coating has a small weight loss interval from 40 to 164.6 °C, with the weight loss being about 4.0%, and the starting thermal decomposition temperature of 95 °C is lower than that of the road marking coating base material (121 °C) and the temperature interval is larger than that of the road marking coating base material, which is mainly due to the evaporation of the water residual in the coating as well as thermal decomposition of a part of the substance and the organosilicon hydrophobic agent. When the temperature continues to rise, the multifunctional coating begins to melt and decompose and then enters the second stage, wherein the weight loss reaches 10.3%, and the thermal stability of the multifunctional coating is improved in this stage, which is not only due to the modified nano  $\text{TiO}_2$  having excellent thermal stability but also because part of the pyrophosphoric acid decomposed by APP reacts with the modified nano  $\text{TiO}_2$  to generate titanium pyrophosphate, which can effectively improve the thermal stability of the system.

The maximum heat loss decomposition temperature in the third stage is 392 °C, and this temperature is the peak of the decomposition temperature of multifunctional coatings, which is 154.3 °C higher than the decomposition temperature of road marking coating base material, which may be due to the addition of nano  $\text{SiO}_2$ , silicone water-repellent agent and its formation of Si-O bonding energy being as high as 4225 kJ/mol, which enhances the heat-resistant properties of multifunctional coatings. The fourth stage is the largest multifunctional coating weight loss stage; the weight loss in this stage is about 12.3% and the maximum thermal weight loss rate is  $-1.5\%/min$ ; the thermal weight loss in this stage is mainly due to the further thermal decomposition of APP into phosphoric acid, metaphosphoric acid, etc., and the decomposition of  $\text{Al}(\text{OH})_3$  to release water from crystallization as well as the organosilicon hydrophobic agent in the decomposition of organic carbonaceous materials at high temperatures to generate carbon dioxide ( $\text{CO}_2$ ) and water. In the fifth stage of multifunctional coating, the weight loss of the coating is less than 1.4%, and the maximum heat weight loss rate is  $-0.2\%/min$ , respectively. During this stage, the weight loss of the coating mainly comes from the decomposition of residual APP and PER.

### 3.1.2. DSC Results Analysis

To study the thermal effect and thermochemical reaction process of multifunctional road marking coatings in tunnels at high temperatures and to further analyze the thermodynamic behavior of multifunctional road marking coatings in tunnels, the marking coatings were analyzed using the DSC test, and since the TG-DTG test found that the marking coatings were accompanied by a change in mass during the thermal decomposition process, the TG curves were further analyzed by placing the TG curves into DSC curves; the results are shown in Figure 5 and Table 2.

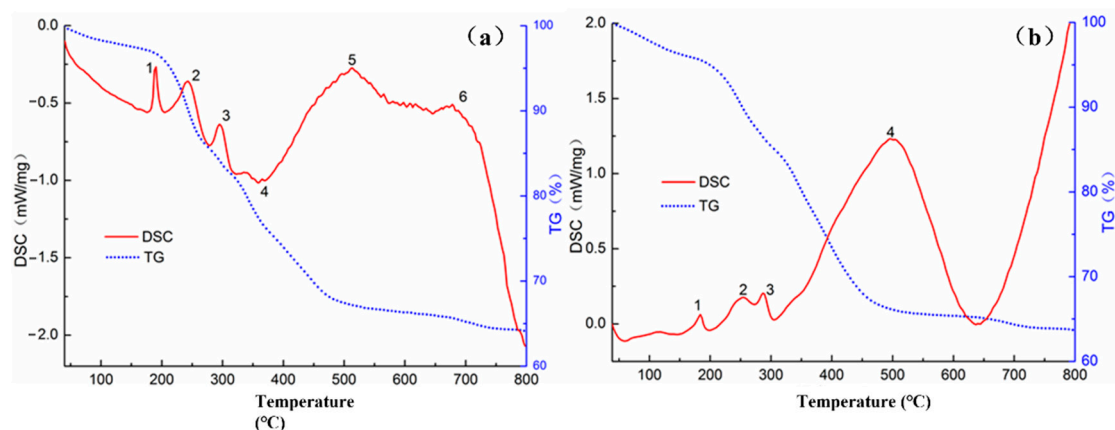


**Figure 5.** DSC curves of multifunctional road marking coatings: (a) base material; (b) modified.

**Table 2.** DSC analysis results of multifunctional road marking coatings: (a) base material; (b) modified.

Materials	Characteristic Peak	Starting Temperature (°C)	Peak Temperature (°C)	Termination Temperature (°C)
(a) Road marking coating base material	1	173	187	208
	2	206	240	278
	3	278	297	316
	4	339	361	420
	5	420	510	572
	6	641	676	716
(b) Multifunctional marking paint	1	143	180	202
	2	202	260	275
	3	275	305	310
	4	310	635	640

From Figure 5a and Table 2(a), it can be seen that the DSC curves of the road marking coating base material have five obvious heat absorption peaks (Peak 1, Peak 2, Peak 3, Peak 5, and Peak 6) and one obvious exothermic peak (Peak 4), in which the heat absorption of Peak 5 is the largest and that of Peak 1, Peak 2 and Peak 3 is smaller. Combined with the results of thermogravimetric analysis, it can be seen that Peak 1 should be the release of the combined water in the coating, generating water vapor generated by the heat absorption. Peak 2 corresponds to the heat absorption peaks of APP and  $\text{Al}(\text{OH})_3$ ; at this time, APP began to absorb heat to release ammonia, water and phosphoric acid, etc., and the decomposition of aluminum hydroxide will also begin to absorb heat to release the water from crystallization and evaporation at high temperatures. Peak 3 corresponds to the peaks in absorption of the heat of the PER and the MEL as well as the APP continuing to absorb heat decomposition, and the generated phosphoric acid reaching about  $300\text{ }^\circ\text{C}$  began to further dehydration to generate pyrophosphoric acid and polyphosphoric acid; due to Peak 4 for the exothermic peak, it can be speculated that in the road marking coating, the base material of the various groups recombines into a new molecular chain segment with the release of heat. Peak 5 of the heat absorption is mainly related to the decomposition of a large number of  $\text{Al}(\text{OH})_3$  in the coating to produce  $\text{Al}_2\text{O}_3$  and water; the small heat absorption peak in Peak 6 is produced when the remaining APP is decomposed.

From Figure 5b and Table 2(b), it can be seen that the DSC curve of the multifunctional road marking coating has four obvious exothermic peaks with the increase in temperature, in which it can be seen that Peak 4 absorbs the largest amount of heat and Peak 3 absorbs the smallest amount of heat; comparing with Figure 5a, it can be seen that, with the incorporation of modified nano  $\text{TiO}_2$  and nano  $\text{SiO}_2$ , it changes the thermal decomposition process of the coating, and there is no obvious exothermic peak, and they improved its high-temperature stability performance overall and did not produce new molecular groups.

Combined with the results of TG analysis, it can be seen that the first three peaks of the multifunctional marking coatings are similar to the base material, mainly due to the evaporation of the combined water in the coating as well as the decomposition of the substrate system's APP, PER and MEL synergistic reaction of heat absorption, and Peak 4 at 635 °C demonstrated a strong heat absorption peak; the stage of absorption of heat is larger, indicating that this stage of the multifunctional marking coatings' thermal stability has the largest contribution, which is mainly due to the multifunctional marking coatings' complex composition system, with PER generating charcoal melting at the same time; the  $\text{Al}(\text{OH})_3$  decomposition reaction is also more active, and APP's further reaction with modified nano  $\text{TiO}_2$  to generate titanium pyrophosphate, etc., absorbs a large amount of heat, with organosilicon water repellent agent with a Si-O bonding energy of 4225 kJ/mol, much greater than the bond energy of the C-C (345 kJ/mol) and C-O bond energy (351 kJ/mol); thus, the breakage of Si-O bond will also absorb heat.

### 3.1.3. Analysis of Combustion Volatiles FTIR Results

In order to study whether toxic gaseous volatiles are generated during the combustion process of multifunctional road marking coatings in tunnels at high temperatures, real-time tracking and detection of the combustion volatiles of multifunctional road marking coatings in tunnels were carried out using FTIR analysis technology; the results are shown in Figure 6.

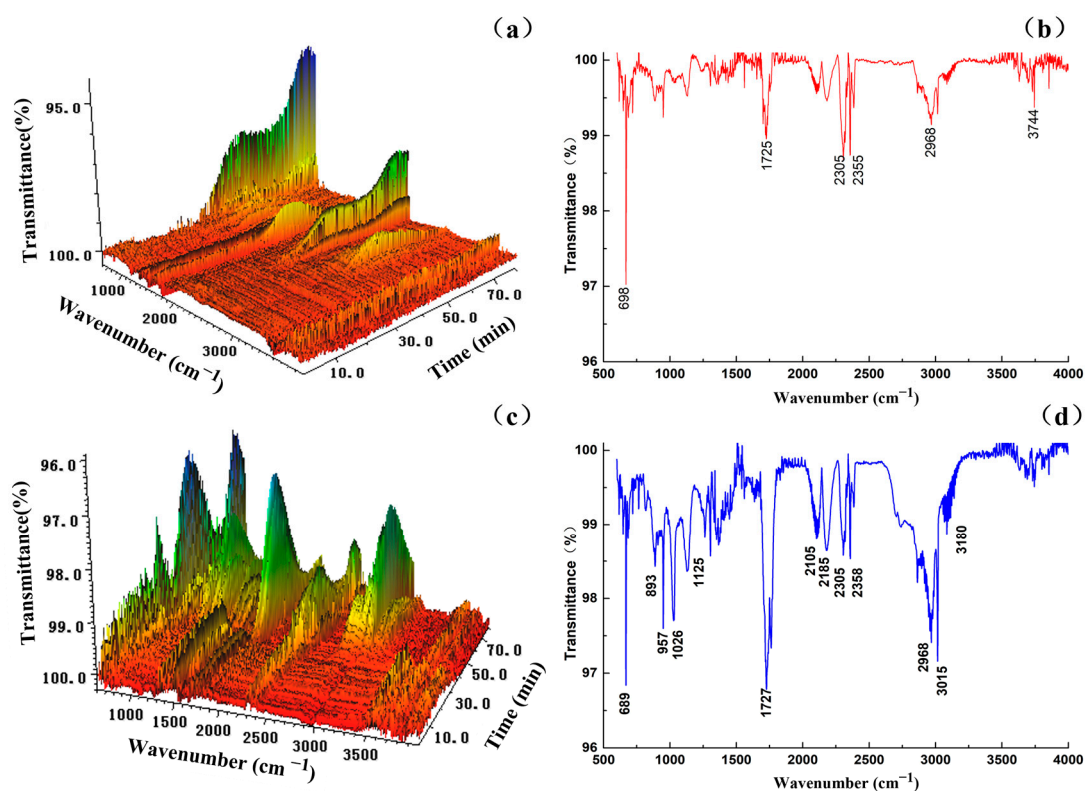


**Figure 6.** D FTIR spectra of volatiles during combustion of multifunctional road marking coatings: (a) base material; (c) modified; (b) 500 °C FTIR spectra; (d) 530 °C FTIR spectra.

From Figure 6a, it can be seen that the road marking coating base material 3D FTIR spectra in the absorption band are weak; only at higher temperatures are there weak peaks, which indicates that the base material combustion process of volatile substances will not produce harmful gases; furthermore, Figure 6c shows that the tunnel multifunctional road marking coatings at 400 °C or below show better thermal stability and almost no volatile substance precipitation, and above, 400 °C there are weak  $\text{CO}_2$ ,  $\text{H}_2\text{O}$  and other characteristic absorption peaks, indicating that adding modified nano  $\text{TiO}_2$  and  $\text{SiO}_2$  to optimize the

thermal stability almost does not produce harmful gases during the combustion process. After 400 °C, there are weak CO<sub>2</sub>, H<sub>2</sub>O, and other characteristic absorption peaks, indicating that the multifunctional road marking coatings with added modified nano TiO<sub>2</sub> and SiO<sub>2</sub> are effective in optimizing the thermal stability during the combustion process and also produce limited amounts of harmful gases.

Considering that the characteristic peaks of volatiles are the most obvious after combustion of the base and modified materials at 500 °C and 530 °C, these two temperatures are chosen for recording the FTIR spectra, and the results are shown in Figure 6b,d. From Figure 6b, it can be seen that the continuous peak appeared at 4000~3500 cm<sup>-1</sup>, which is mainly related to the release of gaseous H<sub>2</sub>O, which is due to the evaporation of the combined water in the multifunctional road marking paint in the tunnel due to the heat and the water generated by the decomposition of Al(OH)<sub>3</sub>. The peaks at 2305 cm<sup>-1</sup> and 2355 cm<sup>-1</sup> are the characteristic absorption peaks of antisymmetric telescopic vibration of CO<sub>2</sub>, which indicates that a certain amount of CO<sub>2</sub> is generated by the combustion of multifunctional road marking coatings in tunnels at high temperatures, and it may be caused by the oxidative decomposition of the base material (a combination of deacidification reaction of carboxylic functional groups and hydroxyl side chain breakage), and the peaks near 2968 cm<sup>-1</sup> are the absorption peaks of methylene symmetric and antisymmetric telescopic vibration caused by the telescopic vibration of the carbonyl group (C=O) at 1725 cm<sup>-1</sup> for the absorption peak of the telescopic vibration of the carbonyl group (C=O); when the carbonyl group undergoes an oxidation reaction, carboxylate groups are generated and heat is released. Therefore, the volatiles released from the base material at high-temperature combustion are mainly CO<sub>2</sub>, H<sub>2</sub>O, and trace amounts of gases containing methylene and carboxyl groups.

Comparing with Figure 6b, it can be seen from Figure 6d and Table 3 that the characteristic peaks of gaseous H<sub>2</sub>O appeared at 4000~3500 cm<sup>-1</sup>, the characteristic absorption peaks due to antisymmetric telescopic vibration of CO<sub>2</sub> appeared at 2305 cm<sup>-1</sup> and 2358 cm<sup>-1</sup>, the characteristic peaks due to methylene symmetry and antisymmetric telescopic vibration appeared near 2968 cm<sup>-1</sup>, with characteristic peaks due to methylene symmetry and antisymmetric telescopic vibration near 2968 cm<sup>-1</sup>, and with the telescopic vibration absorption peak of the carbonyl group (C=O) at 1727 cm<sup>-1</sup>. In addition to this, other weak characteristic peaks also appear; the presence of NH<sub>3</sub> is indicated by the presence of organosilicon hydrophobic agents, nano SiO<sub>2</sub>, and modified nano TiO<sub>2</sub> in the coating, which affect the combustion process of the coating. A stretching vibration absorption peak of -NH- appeared at 3500~3100 cm<sup>-1</sup>, and multiple characteristic absorption peaks (893 cm<sup>-1</sup>, 957 cm<sup>-1</sup>, 1026 cm<sup>-1</sup>) appeared near 1000 cm<sup>-1</sup>, indicating the presence of NH<sub>3</sub>. The characteristic absorption peaks at 2185 cm<sup>-1</sup> and 2105 cm<sup>-1</sup> were caused by the fracture between C=O and C-O-C to produce CO. The reaction of carbonyl (C=O) functional groups removing CO to produce CO<sub>2</sub> is endothermic. Therefore, the volatiles released by the combustion of multifunctional coatings at high temperatures are mainly CO<sub>2</sub>, H<sub>2</sub>O, and NH<sub>3</sub>, as well as trace amounts of gases containing methylene and carboxyl groups, CO, etc.

#### 3.1.4. Micro-Morphological Analysis of the Charcoal Layer after Combustion

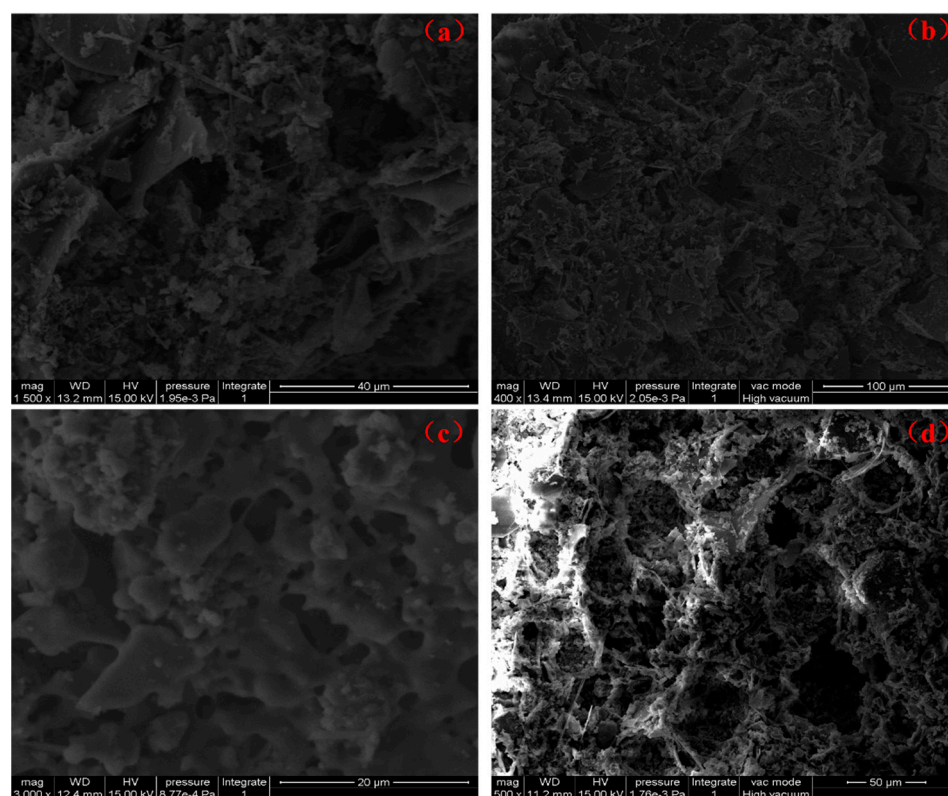
In order to study the protection effect of multifunctional road marking coatings on the base material after high-temperature combustion in tunnels, SEM (scanning electron microscopy) was used to observe the microscopic morphology of the charcoal level; the results are shown in Figure 7.

Figure 7a shows the surface structure of the carbon layer of the road marking coating base material, from which it can be observed that there is a laminar structure, but it is not obvious, and the carbon layer appears to be particularly weak and the laminar structure mostly contains small holes, the reason for which may be the inert gases released by the heat of the coating at high temperatures, which dissipate the laminar structure or break it. Figure 7b shows the fault structure of the carbon layer, from which many irregular honeycomb porous foam structures can be seen, indicating that the cross-section quality of

the carbon layer meets the requirements. Therefore, from the consideration of the carbon layer cross-section and surface directions, it can be concluded that the road marking paint base material has excellent thermal stability.

**Table 3.** Infrared Absorption Frequency Characteristics.

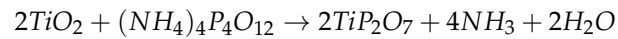
Bond-Type	Type of Vibration	Frequency (cm <sup>-1</sup> )
-NH-	Stretching vibration	3500~3300
O=C=O	Asymmetric stretching vibration	2305, 2358
-C-H-	Symmetric stretching vibration	3300~3000
-C-H	Out-of-plane bending vibration	689
-O-	In-plane bending vibration	1125
-OH	Stretching vibration	4000~3500
-NH	Out-of-plane bending vibration	893, 957
-NH	Deformation vibration	1026
C=O	Stretching vibration	2185
C=O	Conjugate	1740~1700
C-O-C	Stretching vibration	2105
-CH <sub>2</sub> -	Stretching vibration	2968



**Figure 7.** Microscopic morphology of multifunctional road marking coatings: (a) surface of the base material; (b) fault of the base material; (c) surface after modification; (d) fault after modification.

Figure 7c shows the surface structure of the charcoal layer of the multifunctional road marking coating in the tunnel. The surface bubble structure of the charcoal layer is obvious, and the charcoal product is relatively intact in structure, with almost no structural damage and good strength, which is conducive to preventing the escape of inert gases and to improving the thermal stability of the coating. Figure 7d shows the fault structure of the carbon layer of multifunctional road marking paint. From the figure, it can be observed that the carbon fault had an irregular honeycomb porous foam structure; the honeycomb structure was obvious and uniform, and the surface of the carbon layer formed a kind

of white material. Considering this as well as the results of the thermodynamic analysis, it could be argued that this is because of the tunnel multifunctional road marking paint containing modified nano TiO<sub>2</sub>, ammonium polyphosphate, and other ingredients. The modified nano TiO<sub>2</sub> reacts with ammonium polyphosphate at a high temperature to form more stable TiP<sub>2</sub>O<sub>7</sub> (titanium pyrophosphate), and its reaction formula is as follows:

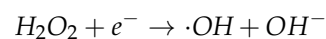
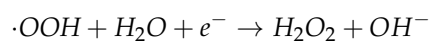
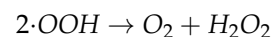
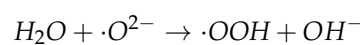
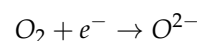


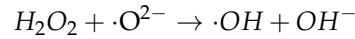
TiP<sub>2</sub>O<sub>7</sub> is a white ceramic-like porous substance, which plays an enhanced role in the skeleton structure of the carbon layer, and the carbon layer does not easily collapse under high temperatures, so the rate of heat loss of the carbon layer decreases significantly, and the antioxidant performance of the carbon layer is obviously improved, which indicates that the addition of modified nano TiO<sub>2</sub> and SiO<sub>2</sub> can enhance its high-temperature stability to a certain extent and optimize its durability. And the more the substance is generated, the more uniform the distribution, the longer the fire resistance limit of the multifunctional road marking coating, and the better the high temperature stability performance, and the TiP<sub>2</sub>O<sub>7</sub> formation process generates a protective gas, NH<sub>3</sub>, that can block the contact between the base material and oxygen. At the same time, the hydrophobic nano SiO<sub>2</sub> in the tunnel multifunctional road marking coatings demonstrates better dispersion, and the coating at high temperatures generated by the charcoal layer containing SiO<sub>2</sub> is also more uniform, which can effectively inhibit the oxygen and heat to the coating of the internal propagation, which improves the tunnel multifunctional road marking coatings' flame-retardant effect. In summary, it can be seen that the surface and cross-section of the modified carbon layer is not only structurally more complete but also generates TiP<sub>2</sub>O<sub>7</sub> ceramic substances conducive to the stability of the coating at high temperatures, which greatly improves the high-temperature resistance of the coating and effectively extends its service life.

#### 4. Assessment of Tail Gas Degradation

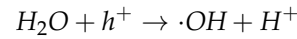
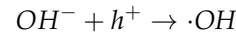
According to the theory of semiconductor solid-state physics, there is a certain band gap in the energy band of TiO<sub>2</sub>, which is between the valence band and conduction band. When the photon energy irradiated on the surface of TiO<sub>2</sub> is equal to or greater than the band gap width (E<sub>g</sub>), the electrical balance between the valence band and conduction band will be lost. An electron (e<sup>-</sup>) in the valence band has an excited transition to the conduction band, the conduction band will have an additional electron (e<sup>-</sup>), and the original valence band will form a hole (h<sup>+</sup>) and, eventually, an electron-hole pair. The electron-hole pair has a strong oxidation-reduction ability, but the life span is very short, and it will migrate to the surface of TiO<sub>2</sub>. During the migration process, (h<sup>+</sup>) and (e<sup>-</sup>) in the electron-hole pair will undergo two changes: first, some electrons (e<sup>-</sup>) and holes (h<sup>+</sup>) will recombine and release heat energy to the outside, making the electron-hole pair lose activity and reducing the photocatalytic efficiency of TiO<sub>2</sub>; second, some electrons (e<sup>-</sup>) and holes (h<sup>+</sup>) are separated and react with O<sub>2</sub> and H<sub>2</sub>O adsorbed on the surface of TiO<sub>2</sub> crystal to form oxidizing agents such as hydroxyl radical (OH), superoxide ion radical (·O<sup>2-</sup>) and ·HO<sub>2</sub> radical.

Studies have shown that when the PH value is less than 4, O<sub>2</sub> adsorbed on the surface of TiO<sub>2</sub> crystal will not only undergo reduction reaction to form hydroxyl radical but will also react with electron (e<sup>-</sup>) to form superoxide ion free radical (·O<sup>2-</sup>).





When the PH value is greater than 10, holes ( $h^+$ ) can oxidize  $OH^-$  and  $H_2O$  adsorbed on the surface of  $TiO_2$  crystal to form hydroxyl radical ( $\cdot OH$ ).



It can be seen from the above chemical reaction formula that the phase-separated electron-hole pair reacts to generate the hydroxyl radical ( $\cdot OH$ ) and superoxide ion ( $\cdot O^{2-}$ ) with strong oxidation during the migration process. These strong oxidants can gradually oxidize organic pollutants and some inorganic pollutants into harmless inorganic small molecules such as  $CO_2$  and  $H_2O$ , so as to achieve the purpose of environmental governance. Therefore, it can be applied in the field of automobile exhaust treatment, and the process of purifying automobile exhaust is shown in Figure 8.

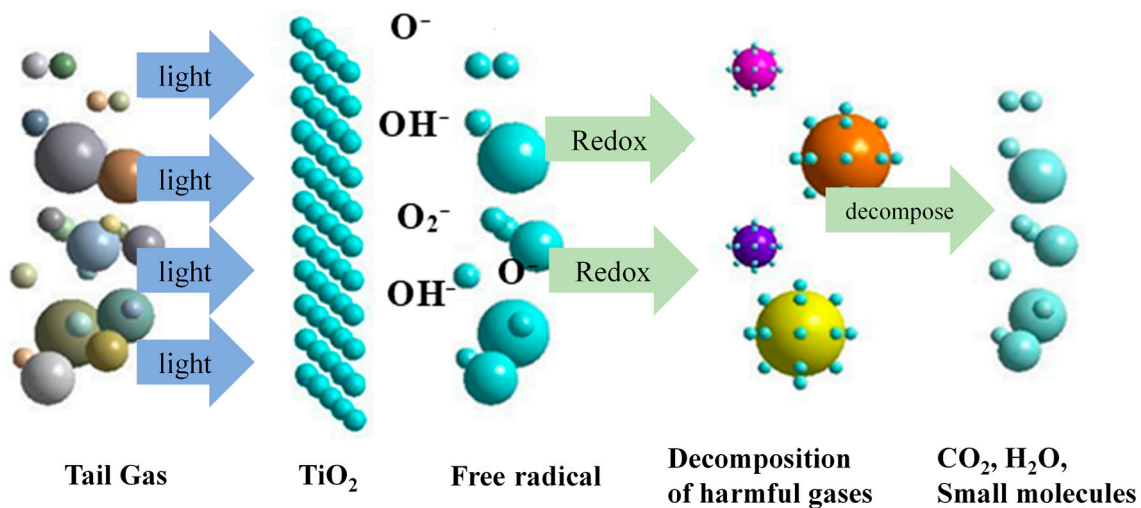


**Figure 8.** Schematic diagram of photocatalytic degradation of automobile exhaust fumes.

To investigate the degradation law of multi-functional road marking coating on four harmful components,  $NO_x$ , HC, CO, and  $CO_2$ , in automobile exhaust fumes in the tunnel, this study presents the degradation law of  $NO_x$ , HC, CO, and  $CO_2$  by taking the change in concentration of harmful components, degradation efficiency  $\eta$  (%) and degradation rate  $k$  as the evaluation indexes, respectively. Among them, the concentration test of harmful components was measured by photocatalyst purification of automobile exhaust test equipment, and the degradation efficiency  $\eta$  (%) was calculated as:

$$\eta = \frac{C_0 - C}{C_0} \times 100\% \quad (1)$$

where  $C_0$  is the initial concentration of the reaction of the harmful components and  $C$  is the concentration of the harmful components after the end of the reaction. The difference between  $C_0$  and  $C$  is the change in the volume concentration of the degraded harmful gases, and the larger the value is, the more obvious the degradation effect of nano  $TiO_2$  is on this kind of gas.

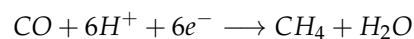
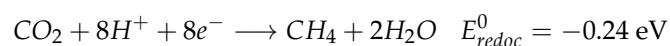
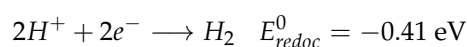
Then, the photocatalytic degradation rate  $k$  on modified nano  $TiO_2$  surface conforms to the Langmuir–Hinshelwood kinetic model:

$$\ln(C/C_0) = -kt \quad (2)$$

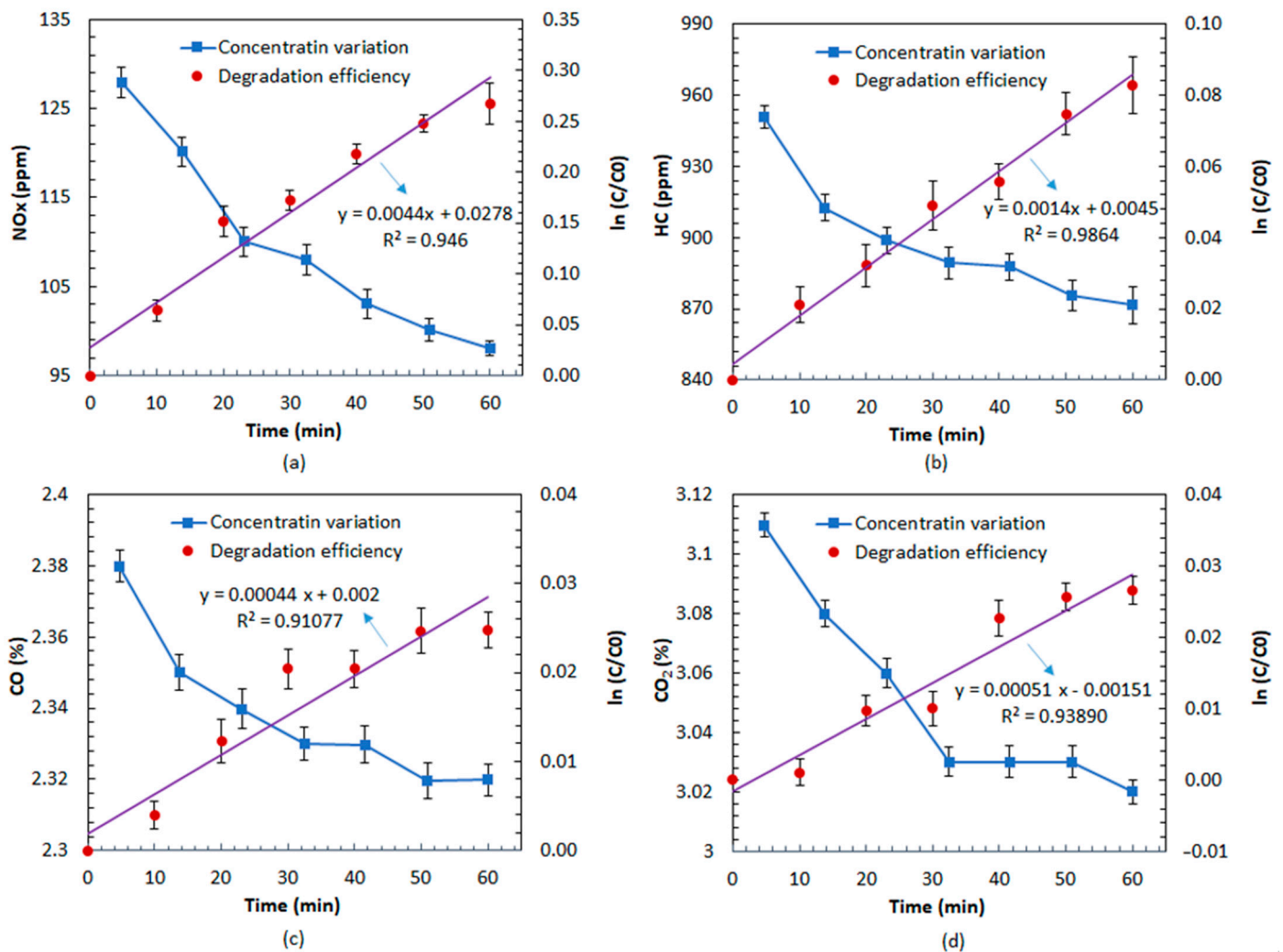
Therefore, the photocatalytic reaction rate constant  $k$  (slope of the fitted straight line) can be calculated by the primary reaction rate (Equation (2)). The size of the photocatalytic reaction rate constant  $k$  reflects the photocatalytic activity, i.e., the larger the value of  $k$ , the higher the efficiency of the photocatalytic reaction.

Figure 9a shows the catalytic degradation of  $\text{NO}_x$  concentration in the exhaust gas with the multifunctional road marking paint in the tunnel. As can be seen from the figure, the concentration of  $\text{NO}_x$  generally shows a decreasing trend with the extension of time, and the  $\text{NO}_x$  concentration decreases faster in the first 20 min at the beginning, after which the decrease rate tends to stabilize. This is because the photocatalytic oxidation process of  $\text{NO}_x$  is  $\text{NO} \rightarrow \text{NO}_2^- \rightarrow \text{NO}_2 \rightarrow \text{NO}_3^-$ , the initial period of multi-functional coatings has physical adsorption of  $\text{NO}_x$ ,  $\text{NO}_x$  is adsorbed on the surface of the coating and the modified nano  $\text{TiO}_2$  on the surface of the coating have better contact, with the degradation of the catalytic reaction and the degradation products of  $\text{NO}_3^-$  adhering to the surface of  $\text{TiO}_2$ , which prevents the photocatalytic reaction from proceeding further. In addition, the high concentration of  $\text{NO}_x$  at the initial stage of the reaction and the decrease in  $\text{NO}_x$  concentration as the reaction proceeds are also factors that affect the  $\text{NO}_x$  degradation rate. Figure 9b shows that the concentration of HC decreases with time because the photocatalytic oxidation process of HC is  $\text{HC} + \text{O}_2 \rightarrow \text{H}_2\text{O} + \text{CO}_3^{2-}$ , which is further decomposed to form  $\text{CO}_2$  and water (a layer of water film is attached to the wall of the reaction box after the experiment), and it is an irreversible process, with the degradation rate being faster at the beginning of the 10 min, and then it tends to be stabilized within 10–60 min. Multifunctional road marking paint in the tunnel under incandescent light can degrade automobile exhaust fumes mainly because the N–V co-doping reduces the forbidden band energy gap of  $\text{TiO}_2$ , widens the range of nano  $\text{TiO}_2$  absorption of visible light, and can absorb more light energy, generating more electron–hole pairs, and the excited state of the electrons are more prone to jump, accelerating the rate of electron interfacial transfer to improve the efficiency of visible photocatalysts so that the coatings have a photocatalytic function. In addition, the degradation rates  $k$  of the four harmful components of automobile exhaust fumes,  $\text{NO}_x$ , HC, CO, and  $\text{CO}_2$ , were  $0.0044 \text{ min}^{-1}$ ,  $0.0014 \text{ min}^{-1}$ ,  $0.00044 \text{ min}^{-1}$ , and  $0.00051 \text{ min}^{-1}$ , respectively.

As shown in Figure 9c,d, it can be seen that the degradation effect of multifunctional road marking paint on CO and  $\text{CO}_2$  in the tunnel is not obvious, and the decrease in the two gases in the first 30 min should be the adsorption effect of the multifunctional paint, with the concentration of CO and  $\text{CO}_2$  being almost unchanged after 30 min. This is because the degradation process of CO and  $\text{CO}_2$  by nano  $\text{TiO}_2$  is mutually reversible, and the specific mechanism is as follows:



The hydrogenation process and hydrogen precipitation process need to consume a lot of electrons and energy, and the priority of their degradation reaction is much lower than that of  $\text{NO}_x$  and HC. Incorporating  $\text{TiO}_2$  nanoparticles into coatings will reduce the photocatalytic performance of  $\text{TiO}_2$  nanoparticles under the influence of other components so that the multifunctional coatings have poorer degradation effects on CO and  $\text{CO}_2$ .



**Figure 9.** Degradation patterns of multifunctional road marking coatings in tunnels on four harmful components of vehicle exhaust: (a) NO<sub>x</sub>; (b) HC; (c) CO; and (d) CO<sub>2</sub>.

Finally, Table 4 shows the degradation efficiency of multifunctional road marking coating in tunnels under incandescent light for the four harmful components of automobile exhaust fumes, NO<sub>x</sub>, HC, CO, and CO<sub>2</sub>. The degradation efficiencies of NO<sub>x</sub>, HC, CO, and CO<sub>2</sub> reached 23.4%, 8.3%, 2.5%, and 2.9%, respectively.

**Table 4.** Degradation efficiency of multifunctional road marking coatings for vehicle exhaust fumes in tunnels.

Exhaust Gas Composition	NO <sub>x</sub>	HC	CO	CO <sub>2</sub>
Photodegradation efficiency (%)	23.4%	8.3%	2.5%	2.9%

#### Self-Cleaning Performance Evaluation

To investigate the self-cleaning performance of multifunctional road marking coating in tunnels, this study adopts the self-cleaning performance test and water droplet contact angle test to obtain the relevant indicators for evaluation. Figure 10 shows the macro-hydrophobicity of multifunctional road marking coating in tunnels; water droplets on the surface of the coating in the testing process present obvious lotus leaf hydrophobic performance, and, after the test, it can be found that the tunnel multifunctional road marking coatings' surface color almost does not change, and no obvious stains are remaining,

according to GB/T31815-2015 in the appendix standards and visual assessment of the test plate of the sewage stain grade: a grade without rainwater stains.

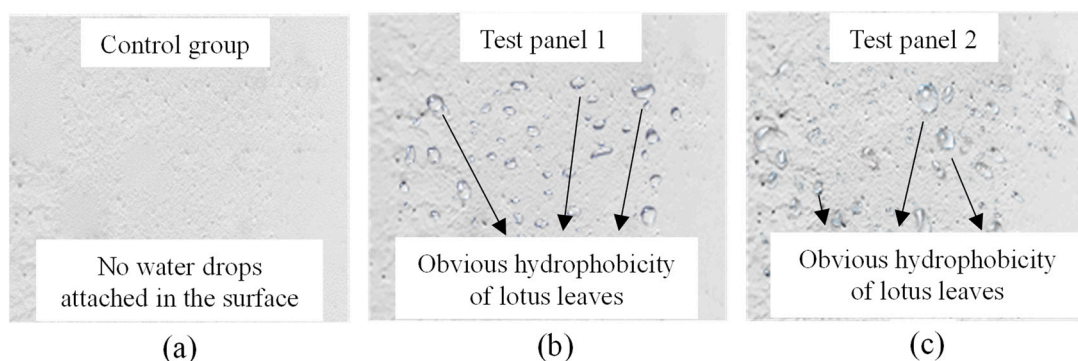


**Figure 10.** Macroscopic hydrophobicity of multifunctional road marking coating in tunnels: (a) comparison panel; (b) test panel 1; (c) test panel 2.

In addition, the SEM microstructure of the surface of the multifunctional road marking coating in the tunnel is demonstrated in Figure 11. The SEM image of the surface of the multifunctional coating at a scale length of 20  $\mu\text{m}$  is shown in Figure 11a. It can be seen that the surface of the multifunctional coating has a high roughness. Protrusions of about 5–30  $\mu\text{m}$  in size are uniformly distributed on the surface, while smaller milky bumps of varying spacings of about 1–4  $\mu\text{m}$  in size are attached to the protrusions. This composite structure is embedded in the interior of the coating in varying degrees, which forms a rough morphology structure similar to that of a volcano. It can also be observed that the distribution of these micrometer-sized protrusions is surrounded by submicrometer-scaled protrusions. This is mainly due to the solid–liquid phase separation in the coating with the evaporation of water, which leads to the formation of the buildup of nanosized  $\text{SiO}_2$  and nanosized  $\text{TiO}_2$  particles on the coating surface, which in turn constructs the composite structure. Figure 11b shows the SEM image in Figure 11a when the scale length is 5  $\mu\text{m}$  after continued magnification. The protrusions have a size of 5–30  $\mu\text{m}$ , and around the protrusions, several hundred-nanometer sub-micron protrusions are uniformly distributed, and tens of nanometers of milky bumps are also attached on the individual sub-micron protrusions. The microstructure of this composite structure is similar to that of the lotus leaf surface, which is a “micrometer–nanometer micro-convex” microstructure. This composite structure is similar to the “micro–nanometer micro-convex” microstructure on the surface of the lotus leaf, which has the effect of bionic self-cleaning.

Finally, the contact angle of the multifunctional road marking coating in tunnels was determined as shown in Figure 12. The contact area between the water droplets and the surface of the multifunctional road marking coating in the tunnel is very small, and the water droplets will slide off the surface of the coating carrier when it is gently shaken. The static hydrophobic angle of the tested water droplets on the coating amounted to 134.2°. Therefore, this multi-functional road marking coating in the tunnel has good hydrophobic performance.

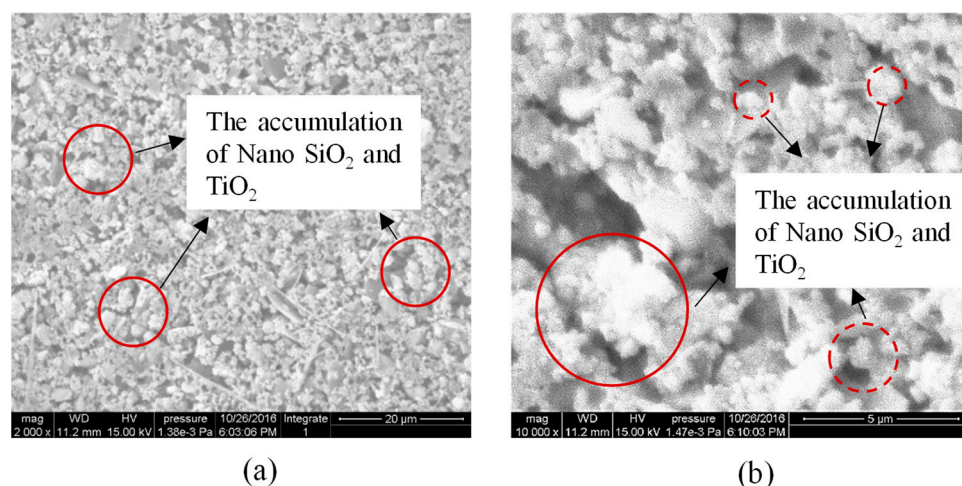


**Figure 11.** Microstructure of the surface of multifunctional road marking coatings in tunnels: (a) scale length of 20 μm; (b) scale length of 5 μm.

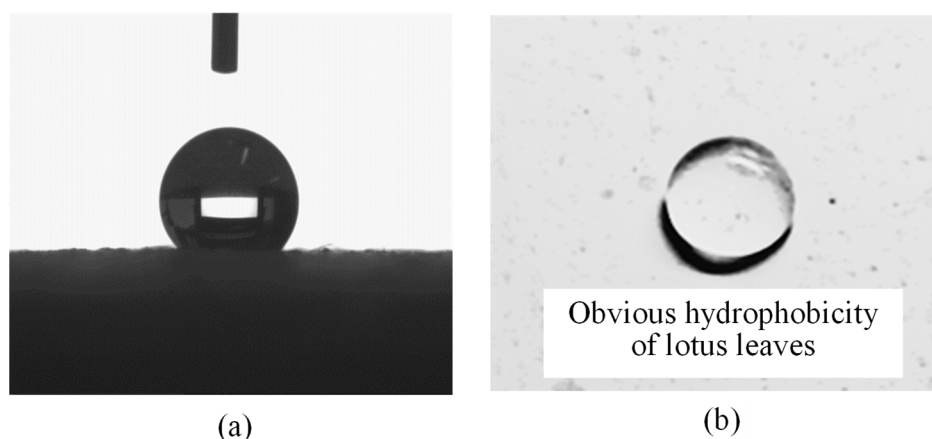


**Figure 12.** Hydrophobicity test of multifunctional road marking coatings in tunnels: (a) contact angle determination graph; (b) water droplets on the coating surface.

## 5. Conclusions

In this study, a two-component road marking material fabricated using active acrylic resin and hydrophobic organosilicon was selected as a base material. Insulation fillers (expanded vermiculite and glass microspheres) and flame-resistant materials (ammonium polyphosphate, pentaerythritol, melamine and aluminum hydroxide) were added into the base marking material. Then, nano SiO<sub>2</sub> and modified nano TiO<sub>2</sub> were added as modifiers to prepare a multifunctional road marking coating for tunnels. The physical and chemical properties of multifunctional road marking coating were evaluating based on laboratory tests including TG-DTG, DSC, FTIR, SEM, exhaust degradation, and contact angle tests, and the main conclusions are as follows:

1. The multifunctional road marking coating in the tunnel developed in this study effectively reduces the thermal conductivity of the carbon layer during the combustion process through the physical changes in the flame retardant system. The heat resistance is formed by nano SiO<sub>2</sub> with high fracture bonding energy and has good high-temperature stability by forming titanium pyrophosphate with a ceramic-like structure with nano TiO<sub>2</sub>, which is conducive to the enhancement of high-temperature stability whilst not producing hazardous volatile gases.
2. N–V co-doping reduces the forbidden band energy gap of TiO<sub>2</sub>, broadens the absorption range of visible light by nano TiO<sub>2</sub>, and improves the catalytic efficiency of visible light. The degradation rates of multifunctional road marking coating in tunnels for

the four harmful components  $\text{NO}_x$ , HC, CO, and  $\text{CO}_2$  in automobile exhaust fumes are  $0.0044 \text{ min}^{-1}$ ,  $0.0014 \text{ min}^{-1}$ ,  $0.00044 \text{ min}^{-1}$ , and  $0.00051 \text{ min}^{-1}$ , respectively. The degradation efficiencies of  $\text{NO}_x$ , HC, CO, and  $\text{CO}_2$  reached 23.4%, 8.3%, 2.5%, and 2.9%, respectively, with better absorption of automobile exhaust.

3. The solid–liquid phase separation in the multifunctional road marking coating in the tunnel causes the nano  $\text{SiO}_2$  and nano  $\text{TiO}_2$  particles to form a pile up on the surface of the paint, which in turn constructs a microstructure similar to the “micro–nanometer micro-convex” on the surface of the lotus leaf. The contact angle of water droplets on the coating surface reaches  $134.2^\circ$ , which has better hydrophobic self-cleaning performance.

Future work will focus on the durability of the developed road marking materials, through the relevant standards to test, compared with the traditional marking materials, so as to apply the long-term service conditions of the road in tunnels.

**Author Contributions:** Study conception and design: L.Y.; data collection: X.Q.; analysis and interpretation of results: Y.C. and S.S.; draft manuscript preparation: H.L. All authors have read and agreed to the published version of the manuscript.

**Funding:** This work was undertaken with funding from the National Natural Science Foundation of China (No. 52108404), Natural Science Foundation of Jiangsu Province (BK20210251) and the fellowship of China Postdoctoral Science Foundation (2021M690613). The opinions, findings, and conclusions expressed in this publication are those of the authors and are not necessarily those of any organization.

**Data Availability Statement:** The data presented in this study are available on request from the corresponding author. The data are not publicly available due to their containing information that could compromise the privacy of research participants.

**Conflicts of Interest:** Author Liang Yang was employed by the company Suqian Highway Business Development Center. The remaining authors declare that the research was conducted in the absence of any commercial or financial relationships that could be construed as a potential conflict of interest.

## References

1. Lu, Y.; Wang, B.; Jiang, J.; Li, H.; Chen, W.; Ye, J. Study on evaluation model of residual bearing capacity of shield tunnel lining structures after fire. *China J. Highw. Transp.* **2023**, 1–18. Available online: <http://kns.cnki.net/kcms/detail/61.1313.U.20231110.0911.004.html> (accessed on 1 February 2024).
2. Chen, H.; Liu, T.; You, X.; Yuan, D.; Ping, Y.; Zhang, Q. Experimental investigation on fire damage to staggered segmental lining of shield tunnel. *Tunn. Undergr. Space Technol.* **2023**, *141*, 105359. [[CrossRef](#)]
3. Li, Q.; Yao, J.; Liang, T. Experimental study on the effect of fireproof coating and cooling methods on the mechanical properties of concrete exposed to high temperature. *Constr. Build. Mater.* **2023**, *376*, 131045. [[CrossRef](#)]
4. Nakamura, T.; Nomura, Y.; Tanaka, A. Study on Spraying Method Using Fireproof Coating Spraying Robot. *AII J. Technol. Des.* **2023**, *29*, 639–644. [[CrossRef](#)]
5. Moosaei, H.R.; Zareei, A.R.; Salemi, N. Elevated Temperature Performance of Concrete Reinforced with Steel, Glass, and Polypropylene Fibers and Fire-proofed with Coating. *Int. J. Eng. Trans. A Basics* **2022**, *35*, 917–930. [[CrossRef](#)]
6. Li, Q.; Li, H.; Liang, T. Effect of non-intumescent fireproof coating on the durability of concrete exposed to elevated temperature. *Constr. Build. Mater.* **2023**, *404*, 133211. [[CrossRef](#)]
7. Wang, Z.F.; Cheng, W.C.; Wang, Y.Q. Investigation into geohazards during urbanization process of Xi’an, China. *Nat. Hazards* **2018**, *92*, 1937–1953. [[CrossRef](#)]
8. Qiao, R.; Shao, Z.; Wei, W.; Zhang, Y.Y. Theoretical Investigation into the Thermo-Mechanical Behaviours of Tunnel Lining during RABT Fire Development. *Arab. J. Sci. Eng.* **2019**, *44*, 4807–4818. [[CrossRef](#)]
9. Zhang, Y.; Weng, X.; Song, Z.; Sun, Y. Modeling of Loess Soaking Induced Impacts on a Metro Tunnel Using a Water Soaking System in Centrifuge. *Geofluids* **2019**, *2019*, 5487952. [[CrossRef](#)]
10. Qiu, J.; Yang, T.; Wang, X.; Wang, L.; Zhang, G. Review of the flame retardancy on highway tunnel asphalt pavement. *Constr. Build. Mater.* **2019**, *195*, 468–482. [[CrossRef](#)]
11. Zheng, Y.; Zhong, H.; Fang, Y.; Zhang, W.; Liu, K.; Fang, J. Rockburst Prediction Model Based on Entropy Weight Integrated with Grey Relational BP Neural Network. *Adv. Civil. Eng.* **2019**, *2019*, 3453614. [[CrossRef](#)]
12. Kim, J.H.J.; Lim, Y.M.; Won, J.P.; Park, H.G. Fire resistant behavior of newly developed bottom-ash-based cementitious coating applied concrete tunnel lining under RABT fire loading. *Constr. Build. Mater.* **2010**, *24*, 1984–1994. [[CrossRef](#)]

13. Alhawat, H.; Hamid, R.; Baharom, S.; Azmi, M.R.; Kaish, A.B.M.A. Thermal behaviour of unloaded concrete tunnel lining through an innovative large-scale tunnel fire experimental testing setup. *Constr. Build. Mater.* **2021**, *283*, 122718. [[CrossRef](#)]
14. Radzi, N.A.M.; Hamid, R.; Mutalib, A.A. A Review of Methods, Issues and Challenges of Small-scale Fire Testing of Tunnel Lining Concrete. *J. Appl. Sci.* **2016**, *16*, 293–301. [[CrossRef](#)]
15. Ibrahim, R.K.; Hamid, R.; Taha, M.R. Fire resistance of high-volume fly ash mortars with nanosilica addition. *Constr. Build. Mater.* **2012**, *36*, 779–786. [[CrossRef](#)]
16. Abhilash, P.P.; Nayak, D.K.; Sangoju, B.; Kumar, R.; Kumar, V. Effect of nano silica in concrete; a review. *Constr. Build. Mater.* **2021**, *278*, 122347. [[CrossRef](#)]
17. Pereyra, A.M.; Canosa, G.; Giudice, C.A. Nanostructured protective coating systems, fireproof and environmentally friendly, suitable for the protection of metallic substrates. *Ind. Eng. Chem. Res.* **2010**, *49*, 2740–2746. [[CrossRef](#)]
18. Zhang, H.J.; Wang, Y.C.; Li, F.; Zhao, J.P. In-situ polymerized zinc phytate chelated Si-C-P geopolymer hybrid coating constructed by incorporating chitosan oligosaccharide and DOPO for flame-retardant plywood. *Constr. Build. Mater.* **2023**, *397*, 132416. [[CrossRef](#)]
19. Ng, Y.H.; Suri, A.; Dasari, A.; Tan, K.H. Thermal decomposition and fire response of non-halogenated polymer-based thermal coatings for concrete structures. *Surf. Coat. Technol.* **2017**, *320*, 396–403. [[CrossRef](#)]
20. Abniki, M.; Shirkavand Hadavand, B.; Najafi, F.; Ghasedi, I. Synthesis of the effective flame retardant via modification of epoxy resin with phenylboronic acid. *J. Macromol. Sci. Part. A* **2022**, *59*, 411–420. [[CrossRef](#)]
21. Wu, J.; Luo, Y.; Qin, Z. Composite-modified nano TiO<sub>2</sub> for the degradation of automobile exhaust in tunnels. *Constr. Build. Mater.* **2023**, *408*, 133805. [[CrossRef](#)]
22. Oliveira, H.G.; Silva, E.D.; Longo, C. Electrochemical and photocatalytic properties of TiO<sub>2</sub>/WO<sub>3</sub> photoelectrodes. In *Solar Hydrogen and Nanotechnology V*; SPIE: San Diego, CA, USA, 2010; Volume 7770, pp. 11–19. [[CrossRef](#)]
23. Luu, C.L.; Nguyen, Q.T.; Ho, S.T. Synthesis and characterization of Fe-doped TiO<sub>2</sub> photocatalyst by the sol-gel method. *Adv. Nat. Sci. Nanosci. Nanotechnol.* **2010**, *1*, 015008. [[CrossRef](#)]
24. Li, Y.; Sun, H.; Peng, T.; You, H.; Zeng, L.; Qin, Y. Preparation and Visible Photocatalytic Properties of N-Doped TiO<sub>2</sub>/Muscovite Nanocomposites. *Clays Clay Miner.* **2021**, *69*, 254–262. [[CrossRef](#)]
25. Zhang, Z.; Liu, K.; Chong, D.; Niu, D.; Lin, P.; Liu, X.; Niu, Y.; Jing, R. Evaluation of photocatalytic micro-surfacing mixture: Road performance, vehicle exhaust gas degradation capacity, and environmental impacts. *Constr. Build. Mater.* **2022**, *345*, 128367. [[CrossRef](#)]
26. Liu, G.; Xia, H.; Niu, Y.; Zhao, X.; Zhang, G.; Song, L.; Chen, H. Photocatalytic performance of doped TiO<sub>2</sub>/AC coating and its UV stability research. *Prog. Org. Coat.* **2020**, *148*, 105882. [[CrossRef](#)]
27. Xia, H.; Liu, G.; Zhang, R.; Song, L.; Chen, H. The photocatalytic degradation of vehicle exhausts by an Fe/N/Co-TiO<sub>2</sub> waterborne coating under visible light. *Materials* **2019**, *12*, 3378. [[CrossRef](#)]
28. Liu, W.; Wang, S.; Zhang, J.; Fan, J. Photocatalytic degradation of vehicle exhausts on asphalt pavement by TiO<sub>2</sub>/rubber composite structure. *Constr. Build. Mater.* **2015**, *81*, 224–232. [[CrossRef](#)]
29. Lu, C.; Zheng, M.; Liu, J.; Zhu, R.; Su, Y. Characterization of self-cleaning pavement coatings with catalytic-hydrophobic synergistic effects. *Constr. Build. Mater.* **2023**, *397*, 132246. [[CrossRef](#)]
30. Jiang, B.; Zu, X.; Tang, F.; Wu, Z.; Lu, J.; Wei, Q.; Zhang, X. Surface modification on nanoscale titanium dioxide by radiation: Preparation and characterization. *J. Appl. Polym. Sci.* **2006**, *100*, 3510–3518. [[CrossRef](#)]
31. Qi, Y.; Chen, S.; Sun, H.; Zhang, J. A multifunctional cool material with contamination-resistant and anti-icing characters based on the application of fluorinated TiO<sub>2</sub>. *Sol. Energy Mater. Sol. Cells* **2019**, *201*, 110091. [[CrossRef](#)]
32. Qi, Y.; Chen, S.; Zhang, J. Fluorine modification on titanium dioxide particles: Improving the anti-icing performance through a very hydrophobic surface. *Appl. Surf. Sci.* **2019**, *476*, 161–173. [[CrossRef](#)]
33. Qi, Y.; Xiang, B.; Zhang, J. Effect of titanium dioxide (TiO<sub>2</sub>) with different crystal forms and surface modifications on cooling property and surface wettability of cool roofing materials. *Sol. Energy Mater. Sol. Cells* **2017**, *172*, 34–43. [[CrossRef](#)]
34. Wang, F.; Zhang, H.; Zhu, H.; Guo, Y. Ultra-hydrophobic modification of TiO<sub>2</sub> nanoparticles via thermal decomposition of polytetrafluoroethylene. *Powder Technol.* **2014**, *253*, 548–552. [[CrossRef](#)]
35. Xi, Y.; Qi, Y.; Mao, Z.; Yang, Z.; Zhang, J. Surface hydrophobic modification of TiO<sub>2</sub> and its application to preparing PMMA/TiO<sub>2</sub> composite cool material with improved hydrophobicity and anti-icing property. *Constr. Build. Mater.* **2021**, *266*, 120916. [[CrossRef](#)]
36. GB/T31815-2015; Self-Cleaning Coatings for Exterior Surfaces of Buildings. Code of China: Beijing, China, 2015.

**Disclaimer/Publisher's Note:** The statements, opinions and data contained in all publications are solely those of the individual author(s) and contributor(s) and not of MDPI and/or the editor(s). MDPI and/or the editor(s) disclaim responsibility for any injury to people or property resulting from any ideas, methods, instructions or products referred to in the content.